

RESEARCH ARTICLE

10.1002/2016JA023700

Key Points:

- A methodology for including anomalous electron heating (AEH) and nonlinear current (NC) enhancement to ionospheric conductance is developed
- Inclusion of AEH and NC affects reduces the cross polar cap potential and improves agreement with DMSP observations
- Inclusion of the AEH and NC effects results in higher inner magnetospheric pressures and improves agreement with D_{ST} and empirical models

Supporting Information:

- Movie S1
- Movie S2

Correspondence to:

M. Wiltberger,
wiltbemj@ucar.edu

Citation:

Wiltberger, M., et al. (2017), Effects of electrojet turbulence on a magnetosphere-ionosphere simulation of a geomagnetic storm, *J. Geophys. Res. Space Physics*, 122, 5008–5027, doi:10.1002/2016JA023700.









Received 16 NOV 2016

Accepted 10 APR 2017

Accepted article online 18 APR 2017

Published online 5 MAY 2017

Effects of electrojet turbulence on a magnetosphere-ionosphere simulation of a geomagnetic storm

M. Wiltberger¹ , V. Merkin² , B. Zhang¹, F. Toffoletto³, M. Oppenheim⁴ , W. Wang¹ , J. G. Lyon⁵ , J. Liu¹ , Y. Dimant⁴ , M. I. Sitnov² , and G. K. Stephens²
¹High Altitude Observatory, National Center for Atmospheric Research, Boulder, Colorado, USA, ²Applied Physics Laboratory, The Johns Hopkins University, Baltimore, Maryland, USA, ³Department of Physics and Astronomy, Rice University, Houston, Texas, USA, ⁴Center for Space Physics, Boston University, Boston, Massachusetts, USA, ⁵Department of Physics and Astronomy, Dartmouth College, Hanover, New Hampshire, USA

Abstract Ionospheric conductance plays an important role in regulating the response of the magnetosphere-ionosphere system to solar wind driving. Typically, models of magnetosphere-ionosphere coupling include changes to ionospheric conductance driven by extreme ultraviolet ionization and electron precipitation. This paper shows that effects driven by the Farley-Buneman instability can also create significant enhancements in the ionospheric conductance, with substantial impacts on geospace. We have implemented a method of including electrojet turbulence (ET) effects into the ionospheric conductance model utilized within geospace simulations. Our particular implementation is tested with simulations of the Lyon-Fedder-Mobarry global magnetosphere model coupled with the Rice Convection Model of the inner magnetosphere. We examine the impact of including ET-modified conductances in a case study of the geomagnetic storm of 17 March 2013. Simulations with ET show a 13% reduction in the cross polar cap potential at the beginning of the storm and up to 20% increases in the Pedersen and Hall conductance. These simulation results show better agreement with Defense Meteorological Satellite Program observations, including capturing features of subauroral polarization streams. The field-aligned current (FAC) patterns show little differences during the peak of storm and agree well with Active Magnetosphere and Planetary Electrodynamics Response Experiment (AMPERE) reconstructions. Typically, the simulated FAC densities are stronger and at slightly higher latitudes than shown by AMPERE. The inner magnetospheric pressures derived from Tsyganenko-Sitnov empirical magnetic field model show that the inclusion of the ET effects increases the peak pressure and brings the results into better agreement with the empirical model.

1. Introduction

The role of ionospheric conductivity in the solar wind-magnetosphere-ionosphere coupling has been recognized for a long time [e.g., *Coroniti and Kennel*, 1973; *Hill et al.*, 1976]. The conductivity allows closure of field-aligned Birkeland currents generated in the magnetosphere and governs the amount and distribution of energy dissipation (Joule heating) in the ionosphere. Due to this current closure, the height-integrated conductivity or ionospheric conductance exerts feedback on the global magnetosphere, affecting such distant regions as the magnetopause and the bow shock [*Merkine et al.*, 2003; *Merkin et al.*, 2005a, 2005b]. Since the conductance is a tensor relating currents and electric fields [e.g., *Kelley*, 1989, p. 45] for a given distribution of the field-aligned currents (FACs), it determines the ionospheric plasma convection and, thus, due to at least partial mapping of electric fields between the ionosphere and magnetosphere, the magnetospheric plasma convection as well. This understanding underlies most models of magnetospheric convection that include magnetosphere-ionosphere coupling [*Wolf*, 1983; *Fedder et al.*, 1995a; *Raeder et al.*, 1995; *Ridley et al.*, 2004; *Merkin and Lyon*, 2010]. Effects of the ionospheric conductance on the magnetosphere have been mainly reported using magnetosphere-ionosphere simulations, and, as shown by many modeling results, it has become rather clear that the ionospheric conductance significantly impacts magnetosphere dynamics. For instance, ionospheric conductance appears as a parameter governing passively [*Siscoe et al.*, 2002a, 2002b] or actively [*Merkine et al.*, 2003; *Merkin et al.*, 2005b] the saturation of the cross polar cap potential (CPCP) in global models through regulation of the FAC strength. *Ridley et al.* [2004] considered in detail effects of

different contributions to the ionospheric conductance, including solar illumination and magnetospheric particle precipitation. The latter, in particular, was also shown to have a major effect on the initiation of substorms in global models [Raeder *et al.*, 2001].

Despite these modeling results, observational evidence for conductance effects on the magnetosphere remains scarce due primarily to the notorious difficulty of directly measuring the ionospheric conductivity. Nevertheless, Ohtani *et al.* [2014] was able to show statistically that the ionospheric FACs depend on the level of the solar irradiance, measured by the $F_{10.7}$ flux, and thus on the dayside ionospheric conductance. Notably, not only the dayside but also the nightside currents responded in the same way to solar cycle variations, i.e., their intensity increased with enhanced solar activity. Ohtani *et al.* [2014] noted that this had significant implications for the global structure of the magnetosphere and the energy and momentum exchange between the solar wind and the magnetosphere.

Conductivity of the ionospheric plasma is typically assumed to be produced by the extreme ultraviolet (EUV) solar radiation and by magnetospheric particle precipitation [Rasmussen *et al.*, 1988; Moen and Brekke, 1993]. These are the processes that are typically included in the calculation of ionospheric convection by magnetospheric models [Fedder *et al.*, 1995b; Janhunen, 1996; Toffoletto *et al.*, 2003; Raeder, 2003; Wiltberger *et al.*, 2009]. However, there are other processes in the ionospheric plasma that can create conductivity but are usually completely ignored in magnetospheric models, e.g., the ionospheric *E* layer microturbulence [Dimant and Oppenheim, 2011a, 2011b]. During active geomagnetic events, such as magnetic storms, strong DC convection electric fields create the high-latitude electrojets in the *E* region ionosphere between 90 and 125 km altitude. These fields drive plasma instabilities, mainly the Farley-Buneman (FB) instability [Buneman, 1963; Farley, 1963]. They generate plasma turbulence that consists of electrostatic field fluctuations coupled to plasma density irregularities [Balsley and Farley, 1971; Cohen and Bowles, 1967; Crochet *et al.*, 1979; Kudeki *et al.*, 1987; Fukao *et al.*, 1998; Pfaff *et al.*, 1987; Rose *et al.*, 1992]. Typical wavelengths of *E* region turbulence are between tens of centimeters and tens of meters, while characteristic wave periods are a few milliseconds [Oppenheim *et al.*, 2008; Kovalev *et al.*, 2008; Oppenheim and Dimant, 2013a; Hassan *et al.*, 2015]. This turbulence modifies the ionospheric conductivities in two ways: (1) It causes anomalous electron heating (AEH), raising the temperatures from between 300 to 500 K up to 4000 K [Bahcivan, 2007; Foster and Erickson, 2000; Providakes *et al.*, 1988; Schlegel and St Maurice, 1981; St Maurice, 1990; Stauning and Olesen, 1989; Liu *et al.*, 2016]; and (2) it drives nonlinear currents (NC) that enhance the ion-dominated Pedersen conductivity [Buchert *et al.*, 2006; Dimant and Oppenheim, 2011a, 2011b; Oppenheim, 1997; Oppenheim and Dimant, 2013b; Rogister and Jamin, 1975].

Anomalous electron heating occurs when the FB instability creates a small turbulent electric field component along the magnetic field [Providakes *et al.*, 1988; St Maurice and Laher, 1985; St Maurice, 1990]. This means that only 3-D models and simulations can evaluate it. A model of AEH that uses the root-mean-square turbulent electric field and density fluctuations and takes into account a feedback of the electron and ion temperature modifications on the threshold electric field has been developed by Dimant and Milikh [2003] and Milikh and Dimant [2002, 2003]. Results of this model showed good agreement with radar measurements of AEH [Milikh and Dimant, 2003]. Strong electron temperature elevations caused by AEH do not affect the ionospheric conductivity directly because the Pedersen current is carried largely by ions, while the Hall current, carried mainly by electrons, is almost temperature independent. However, local AEH increases *E* region electron density due to a partial suppression of the electron-ion recombination rate through electron temperature elevation [Dimant and Milikh, 2003; Gurevich, 1978; Milikh and Dimant, 2003; Milikh *et al.*, 2006; Schlegel, 1982; St Maurice, 1990]. This effect was verified with detailed radar observations [Milikh *et al.*, 2006].

E region turbulence also gives rise to the direct nonlinear current carried mostly by electrons in the Pedersen direction [Oppenheim, 1996, 1997; Dimant and Oppenheim, 2011a]. The NC increases the entire macroscale current, enhancing the total plasma conductivity, especially the crucial Pedersen component as explained in Dimant and Oppenheim [2011b]. The direct NC develops simultaneously with the turbulence, i.e., almost instantaneously, and reaches a similar amplitude to the laminar Pedersen current carried by the ions. Unlike the AEH, the NC directly increases the Pedersen conductivity. Thus, the NC can be expected to change the ionospheric current closure, Joule heating, and the polar cap potential pattern.

An initial effort to include effects of the electrojet turbulence in a global magnetosphere simulation was made by Merkin *et al.* [2005b]. They modified the ionospheric conductance module within the Lyon-Fedder-Mobarry (LFM) global magnetosphere model by including only the AEH contribution in the conductance calculation.

A simplified AEH model was used whereby the classical conductance tensor components were multiplied by a factor proportional to \sqrt{E} , where E is the convective electric field, in regions where $E > 20$ mV/m was satisfied. This dependence approximated well the numerical results by *Milikh and Dimant* [2003] based on the heuristic model of the turbulent electric field by *Dimant and Milikh* [2003]. *Merkin et al.* [2005b] found that the inclusion of this significant source of increased conductivity led to a substantial reduction of the strength of ionospheric convection and a much better agreement with the corresponding observations during the Halloween 2003 geomagnetic storm.

Since the turbulence theory relied on the specification of the background ionosphere and thermosphere, including plasma densities and collision rates, *Merkin et al.* [2005b] used simplified parametric dependencies of the turbulent correction to the conductance as a function of the convective electric field. They noted that a more self-consistent approach would be to incorporate anomalous electron heating and cooling into a first-principles ionosphere-thermosphere model, which would then use that information for improved energy balance. Such an effort has recently been undertaken by *Liu et al.* [2016], who included these effects in the thermosphere-ionosphere electrodynamics global circulation model (TIEGCM). As a result, they obtained a significant increase in the E region electron temperature in the auroral oval and the polar cap of up to a factor of 4, and an increase in Pedersen conductivity of up to 88% relative to the background values without the turbulent corrections.

The ultimate goal of our modeling effort is to combine the improved TIEGCM model with turbulent corrections, including the NC effects, with the LFM global magnetosphere simulations to study global scale effects of ionospheric turbulence. In the present paper, we take a step in that direction although here we do not yet use LFM coupled with TIEGCM. Instead, we implement a parameterized model of the E layer turbulence that is more advanced than the one used by *Merkin et al.* [2005b], in particular, including both AEH and NC effects. This model is then used within the Magnetosphere-Ionosphere Coupler/Solver (MIX) code [*Merkin and Lyon*, 2010], which drives ionospheric convection and specifies the inner boundary condition in the LFM model.

We also employ the version of LFM that is coupled with the Rice Convection Model (RCM) [*Pembroke et al.*, 2012], which is necessary for storm time simulations. Since the inclusion of a stronger ring current pressure leads to increased Region 2 (R2) FACs, this affects the current closure in the ionosphere and, in particular, redistributes plasma convection and electric fields from the polar cap more into the electrojets. This, in turn, spatially relocates the regions where the turbulence corrections operate, since these regions are regulated by the intensity of the convective electric field. These effects, enabled by the inclusion of the RCM model into the global calculations, were missing in our previous, less advanced simulations [*Merkin et al.*, 2005b].

Other modeling groups have coupled inner magnetosphere models, such as the RCM to global magnetohydrodynamic (MHD) simulations for simulating the magnetosphere during storms. *De Zeeuw et al.* [2004] did the initial work coupling the RCM with the Block-Adaptive-Tree-Solarwind-Roe-Upwind-Scheme (BATS-R-US) magnetosphere solution. *Welling and Ridley* [2010] conducted a validation study of the Space Weather Modeling Framework with the RCM coupled to the BATS-R-US MHD magnetosphere model and found good agreement with inner magnetosphere pressures and magnetic field. *Raeder et al.* [2016] used a coupled model that consisted of the OpenGGCM global MHD model, the RCM inner magnetosphere model, and the Coupled Thermosphere Ionosphere Model to simulate the 17 March 2013 geomagnetic storm, which is known to have developed Subauroral Polarization Streams (SAPS). They found that the model reproduced many of the salient features of SAPS, such as the strong northward electric fields and associated ion drifts, as well as the trough in electron density.

The goal of this paper is to explore the effects of ionospheric small-scale electrojet turbulence (ET) on the global structure of the magnetosphere and ionosphere using the LFM-RCM global simulation tool. In particular, we are going to examine the effects of the saturated FB instability through both the NC and AEH. The FB instability occurs at high latitudes when the $|\vec{E} \times \vec{B}|$ speed exceeds the ion acoustic speed by a small amount. We chose the geomagnetic storm of 17 March 2013 as a test bed for these simulations since it was a recent modest storm with both solar wind measurements and a broad range of observations. This allowed us to validate the results of including the effects of ET on the simulation results.

This paper is organized as follows. We begin with a detailed discussion of the LFM-RCM model and the inclusion of the ET effects in section 2. This section finishes with an overview of the 17 March 2013 solar wind conditions and details of the simulation setup. Section 3 presents the simulation results for the runs with

and without the ET implementation and compares the results with Defense Meteorological Satellite Program (DMSP) and Active Magnetosphere and Planetary Electrodynamics Response Experiment (AMPERE) observations. It also compares inner magnetosphere pressures with an empirical model. We finish the paper with a brief discussion of the results and next steps for the research efforts using this new modeling capability.

2. Simulation Setup

This study focuses on using the geomagnetic storm that occurred on 17 March 2013 as a case study for two new features of the LFM-RCM geospace model. As previously discussed, the LFM-RCM model combines the Lyon-Fedder-Mobarry MHD model of the magnetosphere with the Rice Convection Model of the inner magnetosphere and the Magnetosphere-Ionosphere Coupler Solver (MIX) of ionospheric electrodynamics to provide a coupled model of the geospace system. *Pembroke et al.* [2012] describes in detail the basic process of coupling these three models together during idealized solar wind conditions with modest solar wind driving and no dipole tilt. Section 2.1 describes how this approach has been modified to include realistic solar wind conditions, including nonzero interplanetary magnetic field (IMF) B_y , as well as variations in the Earth's dipole tilt. *Merkin et al.* [2005b] implemented an adjustment to the ionospheric conductances based upon the theoretical analysis of the FB instability conducted by *Dimant and Milikh* [2003]. This capability has not been widely used in LFM simulations but is being made part of the LFM-RCM geospace model. Section 2.2 discusses how both the AEH and NC aspects of the electrojet turbulence are implemented in the MIX portion of the LFM-RCM model. And finally, in section 2.3 we present the solar wind conditions for 17 March 2014 and discuss the details of the model setup used for the results presented in the rest of this paper.

2.1. LFM-RCM

Pembroke et al. [2012] provides a detailed description of the coupling process between the LFM, MIX, and RCM models for simulations of geospace. Since that study used idealized solar wind conditions and no dipole tilt, after reviewing the basics of the LFM-RCM coupling, this section will address the changes made to coupling infrastructure needed to allow the model to work for realistic solar wind conditions and dipole tilts.

The fundamental aspect of coupling these models is an exchange of magnetic field and plasma information in the inner magnetosphere to RCM from LFM and then an update of the plasma information from RCM to the LFM. The MIX model is providing ionospheric potential information to both the LFM and RCM models. All of the exchanges use the Center for Integrated Space Weather Modeling coupling infrastructure [Goodrich et al., 2004], and that infrastructure is utilized in the updated version. To transfer information from the LFM to the RCM, the LFM computes time averages of the pressure, density, and magnetic field over an exchange interval. The averaged fields are interpolated using trilinear interpolation onto an intermediate regular Cartesian grid. This intermediate grid is then used to calculate field line-averaged pressure and density for positions on the RCM's ionospheric grid. A key innovation of *Pembroke et al.* [2012] was the implementation of the plasma- β methodology for setting the location of the outer boundary of the RCM. This switch, which essentially prevented the RCM from computing regions with large flows, remains active in the storm simulations we present in this paper. After the RCM computes its plasma pressures and densities, these values are transferred back to the LFM once again using the intermediate grid. The RCM density model includes a modification to a fit of the *Gallagher et al.* [2000] plasmasphere model. At this time we have not implemented a dynamic plasmasphere calculation, but that is a logical next step for improvement of the coupled model. Another set of field line traces from the RCM ionospheric grid points is used to determine the local values on intermediate grid and then those values are interpolated to LFM grid points. The mapping back to LFM assumes that the distribution of plasma density and pressure is constant along field lines. As before, the RCM values do not immediately replace the LFM values; instead, they are slowly bled into the LFM over the exchange time interval. It is important to note that the previous work used a 1 min exchange interval as a balance between speed and accuracy. For strong solar wind driving conditions we have found it necessary to reduce the coupling interval to 15 s in order to ensure stability and prevent the coupled model from producing unrealistically large electric fields in the inner magnetosphere.

The first major modification to the previous coupling efforts is in support of including dipole tilts in the calculation of the coupled model. The LFM-MIX model has long had support for conducting simulations with realistic dipole tilts. This is done by having dipole axis of the Earth aligned with the Z axis of the computational model and inputting the solar wind conditions in solar magnetic (SM) coordinates. *Hapgood* [1992] explains that the SM coordinate system has the Z axis parallel to the north magnetic pole, and the transformation between this

coordinate system and the more commonly used geocentric solar magnetospheric (GSM) coordinate system is simply a rotation about the Y axis by the dipole tilt angle. The Cartesian intermediate grid is set up in SM coordinates for the transfer of data to and from the LFM to RCM. The ionospheric foot points are transformed from geographic coordinates to SM coordinates using the GEOPACK coordinate transform package. The RCM typically includes the effects of the corotation potential, which is not part of the stand-alone LFM-MIX but is enabled when coupled with the RCM.

The second key modification of the LFM-RCM coupling is how the asymmetries in the ionosphere are addressed. In the MIX module the ionospheric potential for the Northern and Southern Hemispheres are calculated independently. The field-aligned current patterns taken from the global MHD simulation are computed for each hemisphere independently, and the ionospheric conductances can be different. The first major difference in the conductance comes from the implementation of an EUV conductance model that calculates the local value of the Hall and Pedersen conductance based upon the solar zenith angle and the $F_{10.7}$ flux value. We have adapted the approach used by assimilative mapping of ionospheric electrodynamics (AMIE) for the MIX module [Richmond, 1992] for the calculation of the EUV conductance. The ionospheric conductance model also includes an empirical model for electron precipitation. As described by Wiltberger *et al.* [2009], this model includes modifications of the precipitation values, based upon the local EUV conductance values allowing the model to simulate seasonal variations of particle precipitation and their impacts on geospace system. On the other hand, the RCM is a 2-D model, which eliminates the field-aligned dimension from the calculation and only requires setting the potential in one hemisphere.

The solution we have adopted for the version of the coupled simulations presented here works as follows. The low-latitude boundary of the ionospheric solution for the electrostatic solver is extended equatorward from 45° to 60° colatitude. The 45° boundary corresponds to dipole mapping of the $2 R_E$ inner boundary of the MHD solution grid within the LFM. For the Northern Hemisphere, the typical low-latitude boundary condition of assuming that potential is zero is used. In the RCM the low-latitude boundary is at 75° colatitude, and in the region between the MIX lower boundary and the RCM lower boundary the electric field supplied to the RCM is set to zero. The northern hemispheric values for the potential, as well as the average energy and flux of precipitating electrons, are then stored for latter passage to the RCM for its calculation. The computation of the Southern Hemisphere potential is done poleward of 45° colatitude with the boundary value being set by the potential obtained from the Northern Hemisphere at that location. By setting the southern hemisphere boundary with the Northern Hemisphere values, we ensure that the potentials from each hemisphere match when mapped to the equatorial plane. This allows for a stable evolution of the coupled model.

2.2. Electrojet Turbulence Implementation

Dimant and Oppenheim [2011b] developed a model of how FB instability modifies E region conductivities when driven by strong DC electric fields. This instability gives rise to both nonlinear currents and anomalous electron heating. Both of these will increase the conductivities. This model was incorporated into the MIX module as a set of conductance correction factors that depend on the driving electric field.

The model of AEH was developed in *Dimant and Milikh* [2003] assuming a specific FB instability level. This self-consistent approach accounts for the fact that as the FB instability raises the electron temperature T_e , it increases the instability threshold on the electric field, $E_{\text{Thr}}^{\text{min}}$, causing the saturated turbulence level to grow with the electric field, E , more slowly than if T_e were constant. It also accounts for kinetic modification of the electron distribution function and the enhanced cooling this causes. The elevated T_e increases both the Pedersen and Hall conductivities by reducing the local plasma recombination rate and therefore increasing the plasma density [Gurevich, 1978; St Maurice, 1990; Dimant and Milikh, 2003; Milikh *et al.*, 2006].

The NC model predicts a nonlinear current driven by the FB turbulence in the direction of the DC field [Oppenheim, 1996, 1997]. This current flows parallel, and with a comparable magnitude, to the fundamental Pedersen current. This develops when FB waves generate perturbed electric fields, causing electrons to $\vec{E} \times \vec{B}$ drift perpendicular to the wave's propagation direction. At the wave's maxima, electrons drift with the same velocity but in the opposite direction as they do at the minima. Since more electrons exist around the maxima than near the minima, a net current results in the direction of the Pedersen current.

The model used in the MIX module combines the effects of both AEH and NC. It assumes a level of saturated FB instability density fluctuations as calculated in the *Oppenheim and Dimant* [2013b] Particle-in-cell

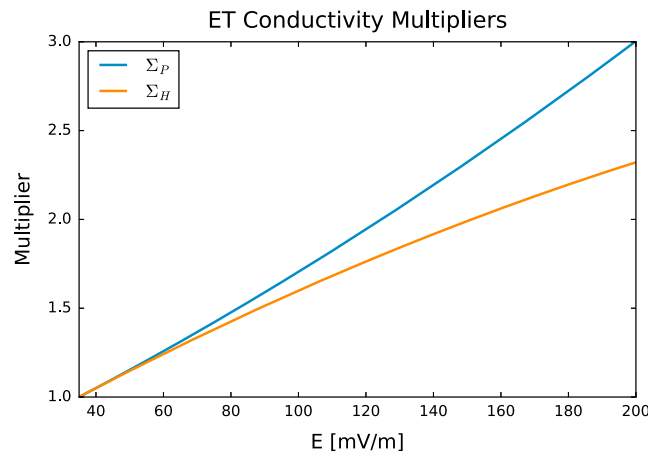


Figure 1. The conductivity multipliers for the electrojet turbulence effects from equations (1) and (2). The blue curve is for the Pedersen conductance; the orange curve is for the Hall conductance. The effects occur for all values above 35 mV/m.

altitude distributions of these quantities in order to calculate simple turbulent correction factors to the laminar conductances. The laminar conductances themselves are calculated within the MIX module, as described in section 2.1. A more accurate and self-consistent model for the nonlinear conductances using more accurate local altitudinal profiles will be implemented in the framework of the combined LFM-TIEGCM-MIX (CMIT) model.

Inside the MIX module we have implemented the following formulations for conductance correction terms to model the combined AEH and NC effects. For the ET-modified Pedersen conductance, Σ_P^{ET} , we utilize

$$\Sigma_P^{ET} = \begin{cases} \Sigma_P^O(1 + 0.01(E - 35) + 1.3 \cdot 10^{-5}(E - 35)^2) & E > 35(\text{mV/m}) \\ \Sigma_P^O & E \leq 35(\text{mV/m}). \end{cases} \quad (1)$$

In equation (1), E is the ionospheric electric field in mV/m and Σ_P^O is the Pedersen conductance obtained from the baseline ionospheric model and includes both the EUV and electron precipitation terms. This multiplier includes the effect of the temperature-driven recombination reduction as well as that of the nonlinear current. The ET-modified Hall conductance, Σ_H^{ET} , is

$$\Sigma_H^{ET} = \begin{cases} \Sigma_H^O(1 + 0.01172(E - 35) - 1.207 \cdot 10^{-5}(E - 35)^2) & E > 35(\text{mV/m}) \\ \Sigma_H^O & E \leq 35(\text{mV/m}) \end{cases} \quad (2)$$

where Σ_H^O is the baseline Hall conductance. Figure 1 shows the effects of these multipliers over a range electric fields. The Pedersen multiplier (blue curve) is nearly linear over the range from 35 to 200 mV/m reaching a peak value of 3.0 at 200 mV/m. The Hall multiplier has a negative coefficient on the squared term and so falls off more dramatically at higher values of the electric field. It reaches a value of 2.3 at 200 mV/m. We note that the FB instability typically starts developing if the convection field, E , exceeds ≈ 20 mV/m. However, the macroscopic effect of E region turbulence becomes substantial only when the field exceeds $E > 35$ mV/m; therefore, we eliminate the effect below this level for computational simplicity.

2.3. 17 March 2013 Simulation

On 17 March 2013 an interplanetary coronal mass ejection (CME) arrived at the Earth and drove a significant geomagnetic storm, $D_{ST} < -100$, over the next day. Solar wind conditions obtained from the OMNI data set were used to drive the LFM-RCM model are shown in Figure 2. Prior to the shock preceding the CME, the solar wind conditions are fairly typical, namely, density $\approx 5/\text{cm}^3$ and velocity ≈ 425 km/s, with IMF weak, < 5 nT in magnitude, mainly in the northward direction. At 05:55 UT a shock is clearly present in the solar wind, with V_X GSM reaching -650 km/s and the density increasing to $10/\text{cm}^3$. In the next 3 h the IMF is variable, with IMF B_Z mainly southward reaching values of -20 nT, but having significant intervals with northward IMF. The Y component of the IMF has similar magnitude in amplitude and appears to have a 180° phase shift.

simulations. This modifies the Hall and Pedersen conductance, as described in *Dimant and Oppenheim* [2011b]. This requires information about the driving electric field and ionospheric temperatures.

Both AEH and the NC predict enhanced conductivities at all locations where turbulence exists. For use in LFM, these must be integrated along magnetic field lines to give conductances. That requires knowing the undisturbed plasma densities and collision rates throughout the turbulent region. This research applies simple averaged ionospheric plasma density profiles and collision frequencies from *Gurevich* [1978]. These averaged models are only needed to mimic typical

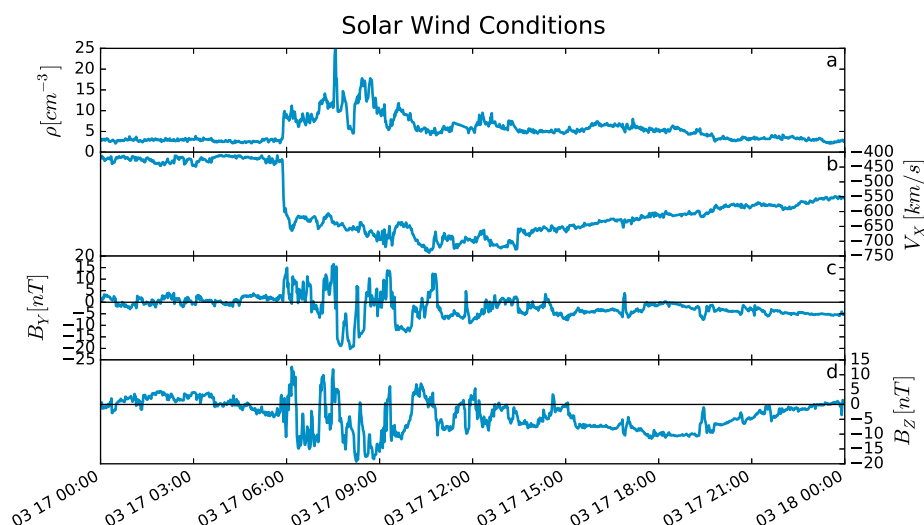


Figure 2. Solar wind and IMF conditions during the 17 March 2013 geomagnetic storm event. (a) The number density; (b) the V_x in GSM coordinates. (c and d) The IMF GSM Y and Z values are plotted.

After approximately 09:00 UT on 17 March 2013 the Y and Z components become more in phase and slowly reduce in amplitude, returning to typical values by the end of the day. After about 12:00 UT the solar wind speed slowly begins to decrease, reaching a value of about 550 km/s by the end of 17 March.

The LFM-RCM simulations for this interval were run using solar wind conditions from Figure 2. The LFM uses a nonorthogonal spherical mesh for the grid. The simulations conducted here use 106 radial, 96 azimuthal, and 128 polar cells. This “quad” resolution version of the LFM contains twice as many cells in each dimension as the results reported by *Pembroke et al.* [2012] initial work with LFM-RCM coupling. The RCM simulations were done on a grid with 200 cells in latitude and 100 cells in longitude and 90 energy channels (28 electron channels, 62 ion (H⁺) channels). The intermediate transfer grid between LFM-RCM used for the field line tracing had a size of $117 \times 110 \times 110$ (x, y, z) points. In the MIX ionospheric solution the ionospheric resolution was increased from a $2 \times 2^\circ$ resolution to $1 \times 1^\circ$ resolution. The full laminar ionospheric conductance model described by *Wiltberger et al.* [2009] was enabled in the MIX calculations. We ran two sets of simulations. The first, hereafter “baseline,” used the standard ionospheric model. The second, hereafter “ET,” had the electrojet turbulence implementation discussed in section 2.2 enabled. The solar wind driving, grid resolution, and all other model parameters are not changed between these two runs.

3. Analysis of Results

We now move on to presenting the results from the two simulations of the St. Patrick’s Day 2013 storm event. We begin section 3.1 with a broad overview of the results of the simulations, with and without the ET effects, including comparisons of ionospheric structures and global measures. After this overview, we move on to making comparisons between the simulation results and observations. In section 3.2 we make detailed comparisons with Defense Meteorological Satellite Program (DMSP) observations during the peak of the storm. These results show the ability of the model to capture features associated with SAPS. Next, we assess the ability of the model to simulate FACs through comparison with FAC patterns derived from AMPERE observations. Finally, in section 3.4, we examine the structure of the inner magnetospheric pressures associated with the ring current by comparing the results with those derived from the TS07d version of the Tsyganenko-Sitnov empirical magnetic field model.

3.1. Baseline Versus ET

Figure 3 is a frame extracted from the scientific visualization that is included in the supporting information that is part of the online version of this article. Figures 3a–3c show the results from the baseline simulation, while Figures 3d–3f show the results from ET simulations. Figures 3a and 3d provide a comparison between the polar cap potential patterns and the structure of the field-aligned currents for the Northern Hemisphere during the course of the magnetic storm. In the snapshot taken at 09:00 UT on 17 March the Region-1 (R1) and Region-2 (R2) FAC current structures are clearly apparent. The CPCP is significantly weaker in the ET run,

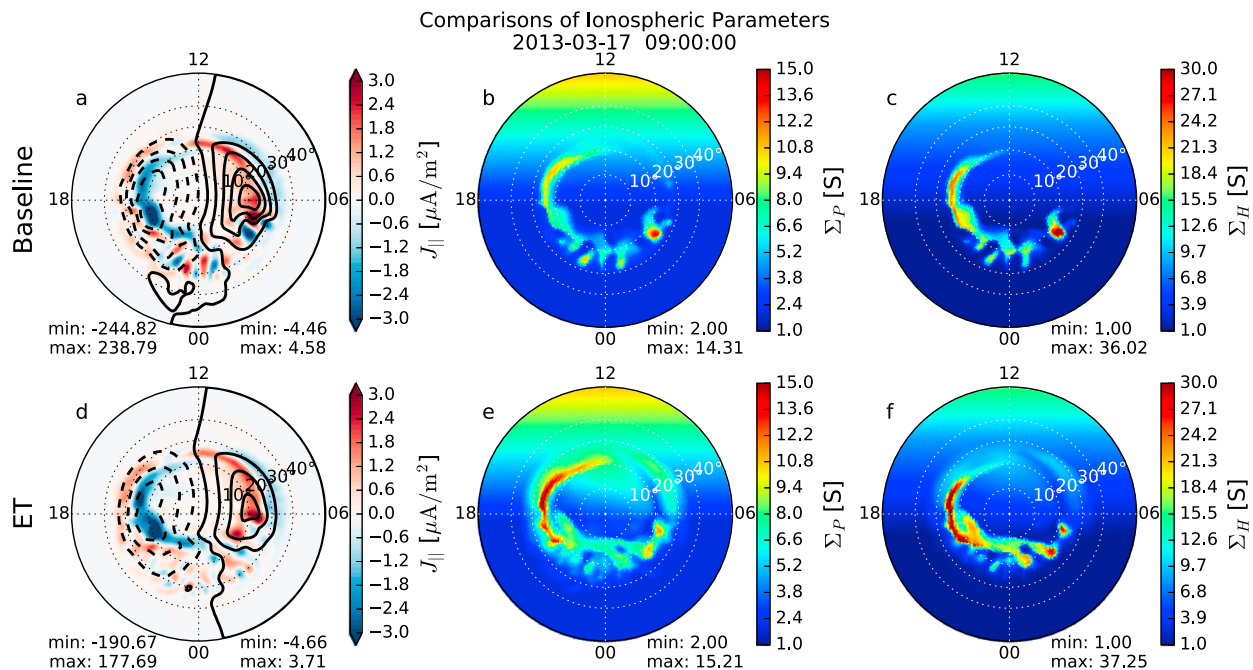


Figure 3. Frame from the scientific visualization showing FAC and polar cap potential, as well as Pedersen and Hall conductivities for the Baseline and ET simulations of the 17 March 2013 geomagnetic storm. Figures 3a–3c (top row) contain results from the baseline simulation, while Figures 3d–3e (bottom row) contain results from the simulation with ET enabled. Figures 3a and 3d has the FAC in color, with blue being upward and red being downward, as well as the polar cap potential pattern with 20 kV contours. Figures 3b and 3e contain the Pedersen conductance. Figures 3c and 3f contain the Hall conductance. Note the Σ_P and Σ_H columns have different color ranges. In each panel the minimum/maximum values for the color-coded values are indicated in the lower right-hand corner. In the first column, the minimum/maximum values for the electric potential are shown in the lower left-hand corner.

but the alignment of the pattern in confinement to high latitudes by the R2 currents is consistent in both simulation results. Figures 3b and 3e show the Pedersen conductance. In both runs the EUV ionization-driven conductance is apparent on the dayside along with auroral oval structure driven by the empirical precipitation model. It is also clear in this snapshot that the ET model is having an impact because the Pedersen conductance in the auroral oval is larger in the ET results. Figures 3c and 3f provide a comparison between the Hall conductances. Just like in the Pedersen conductance, both the EUV-driven and auroral oval pattern are apparent in the Hall conductances. It is important to note, when comparing the conductance plots, that color ranges are the same across simulations for each type of conductance, but the Hall conductance upper limit is larger than the Pedersen conductance by a factor of 2 in order to make the differences between the results more apparent.

Before moving on to the examination of the evolution of the ionospheric parameters in the simulation during the course of the magnetic storm, we turn our attention to Figure 4, which shows a comparison of several global diagnostic parameters over the course of the storm. Figure 4a shows the time history of the CPCP obtained by taking the difference of the max and min of the potential in the Northern Hemisphere at each dump step. Using a convention that will be maintained throughout this paper, the baseline simulation results are shown with the green line and the ET simulation results are shown with the purple line. Figure 4b shows the strength of the field-aligned current obtained by integrating the positive FAC over the Northern Hemisphere at each time step. It also contains the integrated FAC values obtained from the AMPERE measurements with the blue line. Figure 4c shows a comparison between the simulation results and observations for the D_{ST} index. The simulated D_{ST} index was calculated using Biot-Savart method that determines the ground magnetic field perturbations driven by the magnetospheric, field-aligned, and horizontal ionospheric currents. Also shown in this panel is observed D_{ST} index (blue line) obtained from CDAweb database.

The solar wind conditions prior to the 05:50 UT arrival of the shock preceding the CME are modest (see section 2.3 for details). The scientific visualization of the ionospheric parameters begins at 00:00 UT on 17 March, and results shown between them and the arrival of the shock show little difference between the two simulations. For example, at 03:00 UT both simulations show a northward B_z (NBZ) [Zanetti et al., 1984]

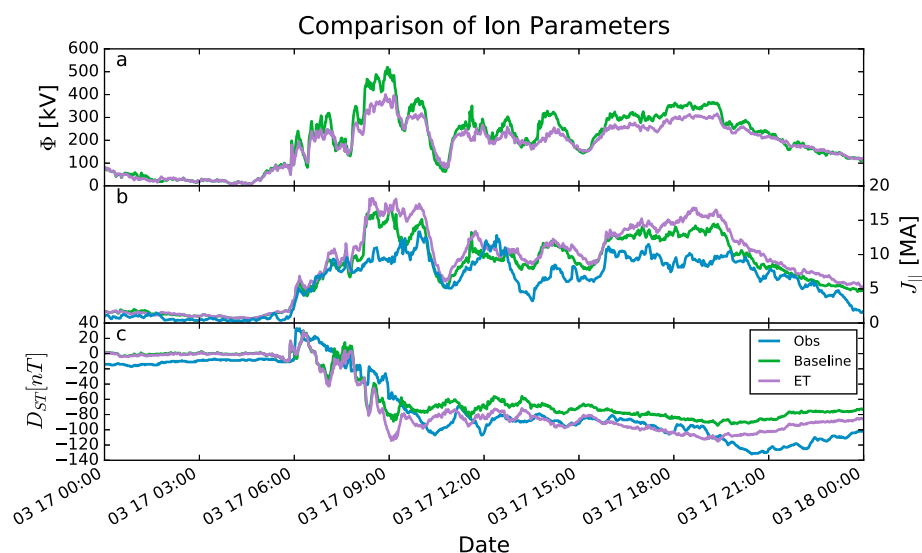


Figure 4. Comparison of the CPCP, integrated FAC, and D_{ST} time series for the storm event for the Northern Hemisphere. (a) The CPCP in kV. (b) The integrated FAC. (c) The D_{ST} index. In each panel the LFM-RCM results are shown with the green line, and the ET results with the purple line. In Figure 4b integrate FAC obtained from AMPERE is plotted in blue. In Figure 4c the D_{ST} obtained from CDAWeb is plotted in blue.

current system in the ionosphere with very weak convection patterns. At this time the main conductance is coming from the EUV ionization and the maximum conductance values in both simulations are identical. In looking at the global diagnostic parameters plotted in Figure 4, the lines for the two simulations are virtually indistinguishable from each other during this interval. This is in line with our expectations that the ET effects will not be activated during typical solar wind conditions when the ionospheric electric field values are less than the 35 mV/m threshold.

After the arrival of the shock the speed exceeds 625 km/s with an initial period of strongly northward IMF followed by a roughly 40 min interval of strongly southward IMF. Between 6:20 and 7:00 UT the IMF B_z component is lower than -10 nT. Combined with the high solar speed, this leads to large CPCPs. The time history of the CPCP and FAC in Figure 4 shows for the first time significant differences in this interval. On average, the CPCP is 12.7% smaller in the ET run than the baseline simulation in this interval. This shows that the inclusion of the ET is having the intended effect of reducing the CPCP during strong driving conditions. During the same interval the FAC is 9.6% larger in the ET run than the baseline simulation, which is consistent with the more conducting ionosphere, allowing stronger FAC currents [Merkin *et al.*, 2005a]. It also shows that there is tight coupling in magnetosphere-ionosphere system, so that one cannot consider the effects of changes in one region in isolation. Looking more closely at the scientific visualization at 07:00 UT, one sees that the most significant differences between the simulated conductances are occurring for the Hall conductance with maximum value 20% higher in the ET run. This enhanced conductance occurs over a large portion of the auroral oval, being most pronounced in the regions near midnight. It is worth pointing out that while the CPCP and integrated FAC have significant differences, visual comparison of the FAC and potential patterns shows considerable agreement between the location of the currents and the alignment of the convection pattern.

After this short period of southward IMF, the IMF turns northward and the disparity between the two simulations is reduced until the next interval of southward IMF arrives at 07:40 UT. With short excursions northward, this period of strong driving lasts until roughly 10:00 UT. During the majority of this interval the IMF is typically lower than -12 nT. Figure 3 shows the comparison between the baseline and ET runs at 09:00 UT, which is in the middle of the interval of strong driving and corresponds to the largest difference between the CPCP seen in Figure 4. While there is not much difference in the maximum in the Hall or Pedersen conductance at this time, there is a clear and significant difference in the conductance patterns. The lack of difference between the maxima is due to the fact that the largest conductance in the baseline simulation is occurring in the region just before dawn, while the similar magnitude maximum is occurring throughout the dusk side in the ET results. The region of significant enhancement in conductance, roughly 3–4 S, begins near 12 MLT and extends to 19 MLT. The high conductivity occurs approximately 15° colatitude and maps to the region between the R1

and R2 currents evident in the FAC patterns. This corresponds to the region of strong electric fields resulting from the current closure. This enhancement is evident in both the Pedersen and Hall conductance panels. Note that this is a qualitative improvement over the previous results by Merkin *et al.* [2005b] where no RCM coupling was implemented, and due to the lack of R2 currents, a larger portion of R1 currents closed over the polar cap. A similar enhancement of the conductance occurs in the prenoon sector. It is occurring at lower latitudes but still maps to the area between the R1 and R2 currents in that sector. There is also an enhancement of the conductance across 00 MLT occurring at high latitudes. It is worth noting that while the CPCP comes into rough agreement during the short northward excursion of the IMF, the integrated FAC are different through and largest at the end of the interval.

As the storm progresses throughout the remainder of the day on 17 March, there are intervals during which the CPCP in the ET run is significantly smaller than in the baseline simulation. Most notable of these are the periods 13:30–14:35 and 15:45–19:30 UT. Both intervals correspond to regions of southward IMF around -7 nT. In the first period the solar speed is near 700 km/s and in the second interval it declines from 625 to 600 km/s. Examination of these intervals reveals structures similar to those shown in Figure 3, especially in the enhancements on the dusk side and prenoon sector between the R1 and R2 currents. It is also instructive to examine the ionospheric patterns at times when there is not a significant difference between the CPCP during the declining phase of the geomagnetic storm. At 13:26 UT, the CPCP and integrated FAC are nearly the same at 180 kV and 9 MA, respectively. The conductance patterns are nearly the same as well with a 1 S difference in the maximum values and enhancement in the conductance in the prenoon and postnoon sectors between the R1 and R2 currents.

As a final comparison between the two simulation results in this section, we turn our attention to the D_{ST} during the geomagnetic storm. Both simulations show positive enhancement of D_{ST} at the arrival of the shock. Between 06:20 and 08:30 UT the simulated D_{ST} indices follow roughly the same path of decreasing value. Both simulations reach an initial minimum D_{ST} value around 09:00 UT, but the ET value is 25 nT smaller than the value obtained by the baseline run. Both simulations reach the minimum value about 90 min before the observations. The 25 nT offset between the ET and baseline runs persists through the remainder of the storm. In the later phases of the storm the observed values come closest to the observations. The simulations are well correlated, both have $R > 0.9$, with observed D_{ST} . The root-mean-square error (RMSE) for the ET run is 5 nT smaller than the baseline run, due mainly to the offset between the simulation results. While not shown here, it is worth pointing out as Li *et al.* [2016] did that LFM-RCM simulations produce a significantly better agreement with D_{ST} than stand-alone LFM simulations.

3.2. Comparison With DMSP

So far the majority of results shown have only contrasted the two simulations. While this is instructive and illustrates the impact that the inclusion of the ET terms is having on the simulation results, it does not provide any verification as to whether the new results are in better agreement with observations. We begin this process by comparing the two simulation results with observations made by the DMSP spacecraft. Figure 5 shows the DMSP F18 trajectories in the Northern Hemisphere during two intervals occurring in the main phase of the geomagnetic storm. The spacecraft was moving from dusk to dawn, measuring the horizontal component of ion drift velocity at altitude of approximately 830 km, together with fluxes of magnetospheric particle precipitation. On the first pass, between 10:10 and 10:20 UT DMSP F18 is passing through the R2 and R1 transition region near 18 MLT. At 10:15 UT in both simulations, the current patterns are quite similar globally and along this portion of the trajectory. In this sector we see that the potential is slightly weaker in the ET results, but globally, the CPCP is slightly higher in the ET results. A bit later in time, during the second DMSP pass, the differences are more pronounced both globally and along the trajectory. At 11:57 UT the baseline simulation has a CPCP that is 11% higher than the ET simulation result.

Figures 6a and 6b show the corresponding comparisons of the cross-track ion drift velocity between the DMSP measurements and the two LFM-RCM simulations along the two consecutive orbits of the F18 spacecraft. The velocity shown in Figure 6 is perpendicular to the satellite trajectory, with negative values for antisunward convection and positive values for sunward convection. The faint lines in Figure 6 show the corresponding energy flux of electron precipitation measured along the two DMSP F18 passes, respectively, together with the simulated energy flux of electron precipitation from the two LFM-RCM simulations. In order to highlight the relationship between the first peak in the cross-track velocity and the auroral oval we have added dashed lines at the time of this velocity peak.

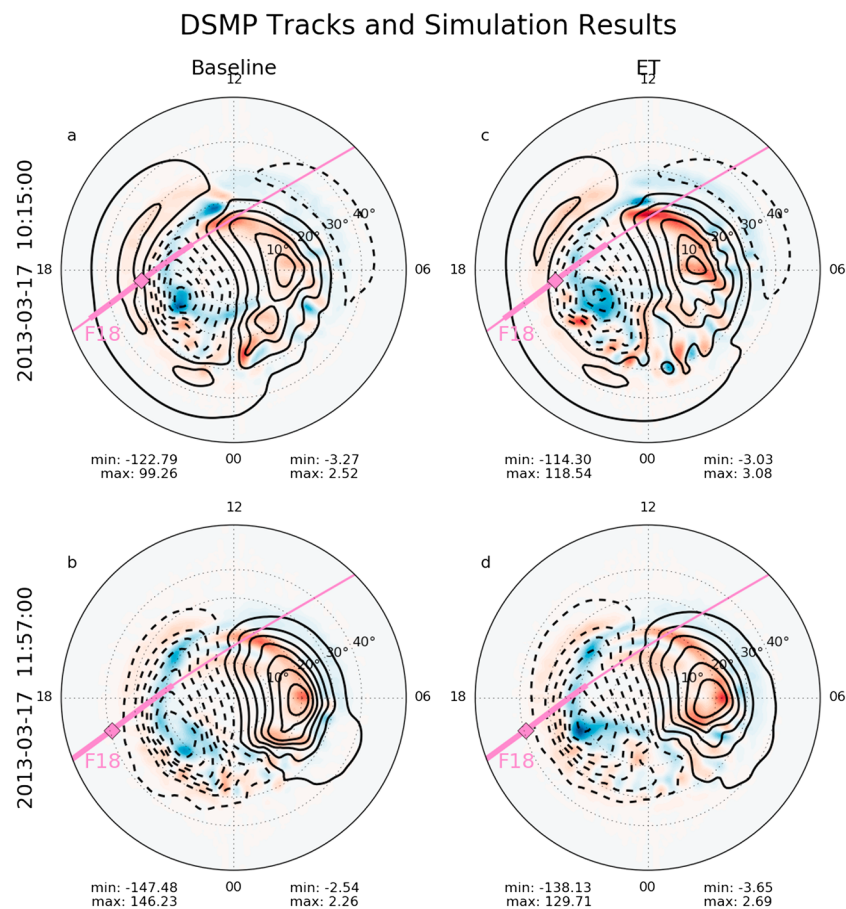


Figure 5. DMSP F18 trajectories overlaid on top of ET FAC and CPCP patterns. The trajectory between 10:00 and 10:45 UT on top of the FAC and CPCP patterns from the (a) baseline and (c) ET simulation results of 10:15 UT. The F18 trajectory between 11:45 and 12:30 UT (b) showing the baseline results and (d) showing the ET results at 11:57 UT. In each panel the wider portion of the trajectory shows the location of the spacecraft in the interval plotted in Figure 6.

The data-model comparisons on the first F18 pass shown in Figure 6a suggest that with the ET module switched on, the LFM-RCM is capable of reproducing the double-channel convection profiles between 10:10 and 10:20, while the standard LFM-RCM simulation does not show a clear double-peak signature along the first F18 trajectory. The DMSP observations show a peak in velocity around 10:13 UT, well before increase in electron energy flux indicative of the auroral oval. At 10:15 a second peak in the velocity overlaps the auroral energy flux. Since the first peak ion flow is at lower latitudes than the auroral energy flux, we interpret this westward ion flow as being a signature of SAPS. The ET simulation results show a similar two-peaked velocity profile at higher latitudes than the DMSP observations. In the baseline simulation the second peak is not as clear, but the profile does level off before dropping, which is also in qualitative agreement with the DMSP F18 observation. While these features are occurring about 4 to 5° further poleward in the simulation results, it is important to note that in both simulations, the first velocity peak is occurring at latitudes equatorward of the auroral energy flux, suggesting that the simulated plasma flow is part of a SAPS channel. The disagreement in the location of the auroral oval is likely a consequence of the fact that the distribution of upward R1 field-aligned currents in the global simulation is several degrees in magnetic latitude poleward when compared to the observations [Zhang *et al.*, 2011]. Consistent with the global picture illustrated in Figures 5a–5c, there is little difference in the peak ion velocity in the two simulation results. Note that in Figure 6a, the DMSP convection speed in the SAPS region exceeds that in either simulation. However, the simulated CPCP at this time is still higher than typically observed. This underscores the fact that large CPCP does not necessarily lead to high convection speeds globally. It is worth noting that similar to that in the observations, the first peak of westward ion drifts occurs in the subauroral region before the occurrence of electron energy flux at

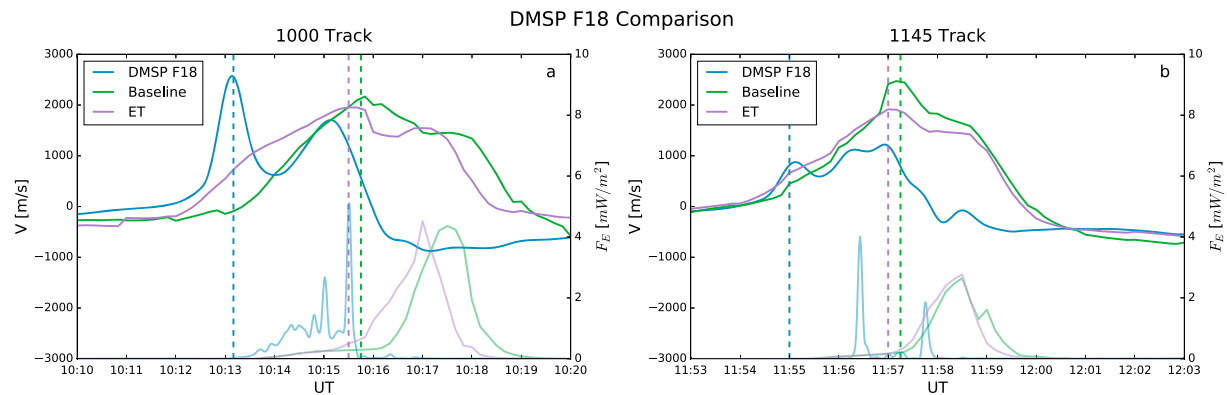


Figure 6. Comparison for DMSP F18 observations and simulation results. (a) The comparison for a portion of 10:00 UT pass and (b) the results for a portion of the 11:45 pass. For each parameter plotted, the DMSP observations are shown in blue, baseline simulation in green and the ET results in purple. The cross-track velocity comparison uses the right y axis and dark color lines. The electron energy flux comparison uses the right y axis and light colored lines. The dashed lines indicate the time of the first peak in the cross-track velocity.

10:16UT in both simulations. This is consistent with the observations that the equatorial ion velocity peak in the subauroral region is most likely associated with the SAPS.

The comparison between the simulation results and the second DMSP pass shown in Figure 6b presents a similar view to the first pass. The first peak in the velocity occurs equatorward of the electron energy flux in both the observations and simulation results. The simulation results are shifted poleward by a similar amount. In both simulations the formation of clear second peak is missing, but they both exhibit the leveling off features seen in the baseline simulation results of the first pass. Consistent with globally weaker CPCP at this time, the ET simulation results have a lower cross-track ion velocity, which is in better agreement with the DMSP observations. Note that the data-model comparisons on both DMSP F18 passes show that the coupled LFM-RCM simulations are capable of reproducing key features of SAPS. With the ET capabilities enabled, the two-peaked feature is more clear in the first pass and the magnitude of the drift velocity agrees more with the observations.

Before moving on, it is instructive to more globally compare the relationship between the electric fields in the high-latitude polar cap and auroral electron energy flux. Figure 7 displays these quantities for the baseline (a) and ET (b) simulations at 10:00 UT. Since the ET module reduces the CPCP, the electric field in the ET simulation is weaker than the baseline simulation. In both LFM-RCM simulations, intense electric fields at magnetic

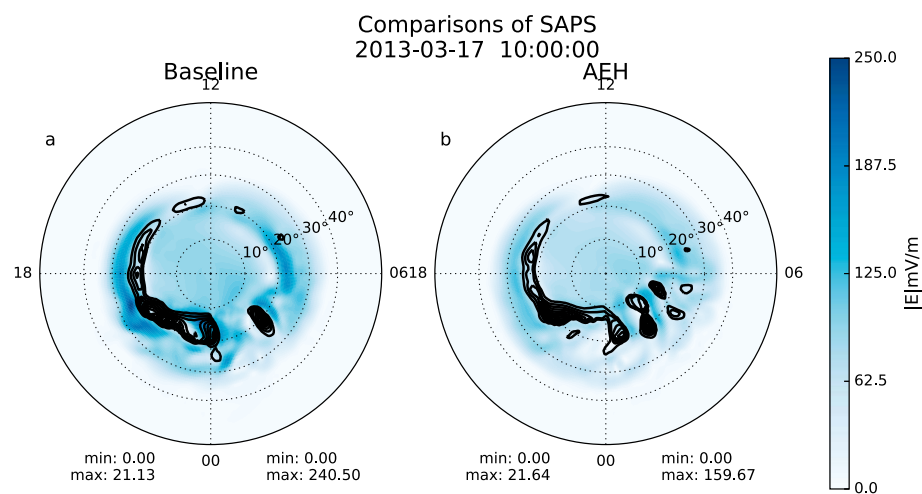


Figure 7. Comparison for electric field magnitude and electron energy flux for the baseline and ET simulation results for 10:00 UT. (a) The results for the baseline simulation; (b) the results for the ET simulation. The blue color shows the intensity of the electric field on the same color table across each plot. The contour lines indicate intensity of electron energy flux with the same contour interval.

latitudes below the auroral electron energy flux in the afternoon and evening sectors are evident, suggesting that the ET module is not a major driver of the SAPS features seen in the simulations. In both simulations, the peak electric field magnitudes occur in the region equatorward of the auroral energy flux, which is consistent with the overall picture of SAPS and regular high-latitude convection electric fields. While not shown here, we have looked at the component breakdown of the electric field in these sectors, and it is almost entirely coming from the meridional component of the electric field. We interpret this as a signature of SAPS throughout both of these sectors.

In the LFM-RCM simulations, the subsequent buildup of large inner magnetospheric pressure gradient and partial ring current (not shown) during the storm time drive downward R2 FACs flowing into the duskside ionosphere (Figure 5). The R2 FACs flow poleward as Pedersen currents through the subauroral ionosphere and emerge as upward R1 FAC in the electron precipitation region. Due to the low conductivity in the duskside ionosphere regions with R2 currents, the poleward Pedersen current generates an intense electric field in order to maintain the continuity of current, which drive fast westward plasma flow in the subauroral region. Therefore, it is the inner magnetosphere model RCM that drives the fast westward plasma flow in the coupled simulations rather than the ET module. Note that without a physics-based ionosphere-thermosphere general circulation model, the midlatitude trough region is not modeled self-consistently in the LFM-RCM simulations, which may have impacts on the global dynamics of SAPS simulations.

3.3. Comparison With AMPERE

Now we move onto a comparison of the simulation results with the observations of the FAC patterns obtained from the AMPERE mission. We begin this comparison by returning briefly to Figure 4 to discuss the comparison of simulation results with the integrated AMPERE FAC values during the course of the storm. Both simulations have correlation coefficients greater than 0.9 with the AMPERE-derived integrated FAC strength. Further, cross-correlation calculations show essentially no lag between the observations and simulation results. The RMSE for the baseline simulation is 1 MA less than the ET simulation results. We interpret these results as showing that the inclusion of the ET effects is not dramatically altering the temporal evolution of the currents, likely due to the direct driving of the R1 currents by the solar wind. As we will discuss in greater detail, Anderson *et al.* [2016] report that AMPERE the reconstruction of the FAC densities from the AMPERE observations likely underestimates total current strength, and so it is possible that the simulation results are within the uncertainty of the method.

The second scientific visualization accompanying this paper makes this comparison by plotting the patterns of the Northern Hemisphere currents along with cuts along specific MLTs. Figure 8 is extracted from this visualization at 09:00 UT on 17 March. Figure 8 (top row) provides a comparison of the FAC patterns for the Northern Hemisphere from the simulation and the AMPERE reconstruction. A 2 min cadence was adopted for this visualization to match the highest output frequency available for the AMPERE observations. It is important to note that the AMPERE observations are built up over a 10 min window and that accumulated pattern is being compared with an instantaneous value obtained from the model output. In order to allow for a more quantitative comparison, Figure 8 (bottom row) contains cuts from the current densities at several magnetic local times. Figures 8d and 8f provide cuts through the morning and afternoon sectors, while Figure 8e provides a cut from dusk to dawn.

As discussed in section 3.1, prior to the arrival of the shock, the solar wind driving of the magnetosphere is quite weak. At 03:00 UT the IMF is mainly northward and a careful examination of the FAC patterns at this time shows an NBZ current system in both simulation results. The faint trace of an NBZ current system is apparent in the afternoon sector in the AMPERE-derived pattern. These patterns can be hard to see in the visualization since the range of the color bar was selected to capture times when strong currents are flowing. Turning our attention to the MLT comparisons we see that for the 09 and 15 MLT cuts, the two simulation results are virtually identical. Differences can be seen in the 18 MLT portion of the dawn-dusk cut, due to the current in the ET version extending slightly more antisunward. The NBZ current systems do not appear in the AMPERE reconstruction, especially since an intensity of $0.15 \mu\text{A m}^{-2}$ is needed for the currents to be above the noise threshold. The strong level of agreement between the two simulations is not surprising since the ET effects are not likely to occur at this point in the simulation.

Next we focus our attention at 09:00 UT shown in Figure 8. It corresponds to the time with the largest differences in the CPCP seen between the two simulation results. While the difference between the CPCP is quite large at this time, FAC patterns for the two simulations are similar, particularly on the dayside in terms of their

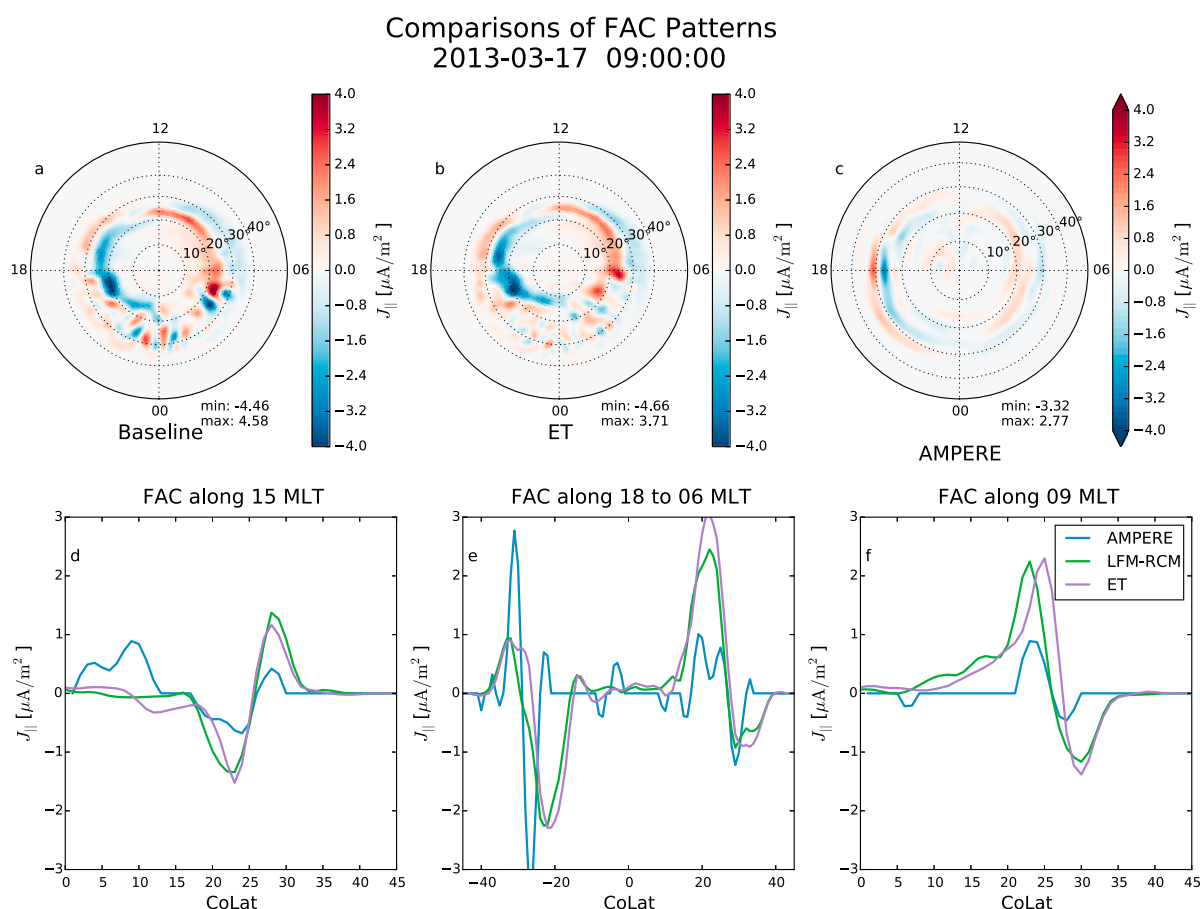


Figure 8. Frame extracted from the scientific visualization comparing the FAC from the simulations with the patterns derived from AMPERE magnetometer observations. (a–c) The FAC patterns for the Northern Hemisphere using the same color bar. (a) The baseline simulation, (b) the electrojet turbulence simulation, and (c) the AMPERE observations. Comparisons of current strengths along cuts in MLT are shown in Figures 8d–8f. (d) A cut along 15 MLT and extends from 0–45° colatitude. (f) A cut along 09 MLT and has the same range as Figure 8a. (e) A cut along the 18 and 06 MLT line. In this plot the negative colatitude values correspond to locations along the 18 MLT line, while the positive values are along the 06 MLT line. This plot gives a cut from dusk to dawn in a single panel. In all the comparison plots the AMPERE observations are shown in blue, the baseline simulation in green, and the ET simulation in purple.

location, width, and strengths of the R1 and R2 current densities. There is a notable difference on the night-side, with the baseline simulation having stronger FAC pairs in the midnight sector. Also, the peaks in the R1 currents that occur below the 18–06 MLT line are stronger in the baseline simulation. The strength of the currents is stronger than those seen in the AMPERE results. The R1 and R2 currents also appear to be at higher latitudes than those seen in the AMPERE results. The weaker current density in the AMPERE results has been reported before by *Merkin et al.* [2013] and *Anderson et al.* [2016]. As these authors report, the main factor contributing the underestimation is the order of the spherical cap harmonic fit, which limits the latitudinal resolution in the AMPERE reconstruction to 2°. When the spacecraft encounters FAC structures that are narrower than this, the densities obtained from the reconstruction will likely be underestimated. It is also possible that the simulation results are overestimating the current densities and that could be determined by a comparing the individual spacecraft measurements of the magnetic field perturbations, but we have elected not to include that labor-intensive comparison in this initial results paper. A reader interested in the process for conducting this comparison is directed to *Merkin et al.* [2013].

Looking at the 15 MLT comparison, we see that the strength of currents along this cut is similar in the baseline and ET simulations. The current density peaks are higher and about 1–2° poleward of those in AMPERE. In the 09 MLT there is a 1–2° difference in the location of the peak current between the two simulation results. The current density peaks in the two simulations appear to bracket the observed current density peak with the baseline simulation peak at above the AMPERE peak and the ET peak below it. The peak current density here is about a factor of 2 larger than the AMPERE results, and the current densities structures are wider.

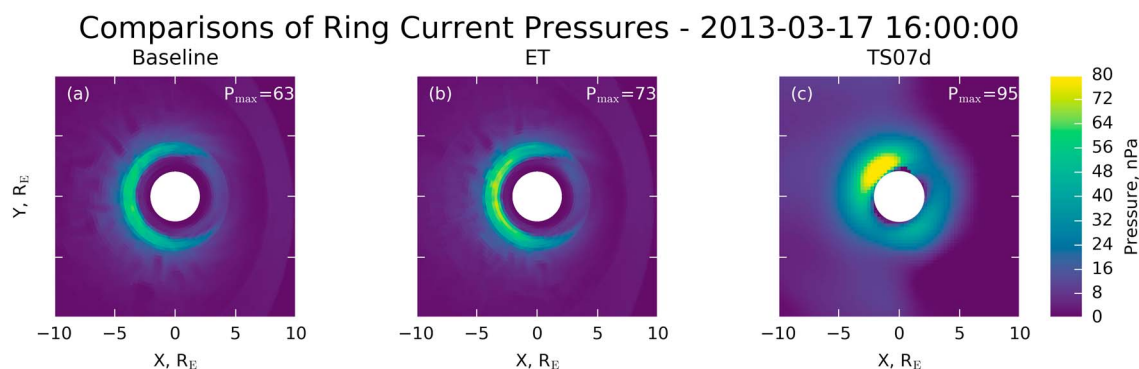


Figure 9. Inner magnetospheric pressures from simulations are compared with results from the TS07d empirical model. (a) The results from the baseline simulation, (b) ET simulations, and (c) the TS07d pressures. In each panel the peak pressure value is displayed in the upper right-hand corner. All plots share the same color bar and view.

The wider current density structures in the simulation results are also seen in the 18–06 MLT cut. This is especially clear for the current densities in the 18 MLT line. Unlike the other current densities reported here, the AMPERE current densities are stronger in this region. Along the 06 MLT cut the current densities return to being about a factor of 2 larger in the R1 location. At this time the CPCP differences between the simulations are significant; however, the difference between the currents in the two simulations is relatively modest. Furthermore, both simulations agree quite well with the AMPERE observations.

As the storm progresses through the remainder of the day, there are intervals with strong solar wind driving that result in significant differences in the simulated CPCP. The 14:00 UT frame is typical of the conditions seen during the 13:30–14:35 interval of strong driving. The modest $1\text{--}2^\circ$ separation between the current peaks noted in the 09 MLT cut of the 09:00 UT results is present in all of the cuts through the currents. In general, the baseline simulation peak appears to be closer to the peak in the AMPERE observations than the ET simulation results. This trend is also apparent in the 15:45–19:30 UT interval of strong driving with the 16:12 frame providing a clear example. Also notable in this frame are the strong peaks in the R1 currents below the 18–06 MLT line in the ET simulation results. It is worth pointing out that at 13:26 UT, previously identified as an instant with little differences between the CPCP and integrated FAC, there are very small differences between the two simulation results.

3.4. Comparison With TS07d

In this final section we turn our focus to the magnetosphere and make a comparison between the simulation results derived from the TS07d empirical magnetic field model *Tsyganenko and Sitnov* [2007]; *Sitnov et al.* [2008]. TS07d differs from classic Tsyganenko magnetic field models [e.g., *Tsyganenko*, 1995], because it presents the magnetic field of equatorial currents using a system of basis functions, whose number can be increased to improve the models ability to resolve progressively finer structures. This new reconstruction technique allowed for the first time to resolve the eastward ring current [Stephens et al., 2016] near Earth, which is critical for correctly capturing the location and magnitude of the ring current pressure peak. The pressure reconstruction procedure using the isotropic force balance condition $\vec{J} \times \vec{B} = -\nabla P$ was described in detail by *Sergeev et al.* [1994] and then applied to reconstruct the pressure distributions on the basis of the TS07d by *Stephens et al.* [2013].

Figure 9 presents this comparison for the baseline (a) and ET (b) simulations with the TS07d (c) results for 16:00 UT on 17 March. The data are extracted from the SM equatorial plane and compared with the GSM equatorial in the TS07d results. At 16:00 UT the dipole tilt angle is only 8.4° , so the differences between these planes close to the Earth will be small. We selected 16:00 UT as the time for this comparison because it is during the recovery phase and the ring current is expected to be well established. The white circle in the LFM-RCM plots represents the $2 R_E$ inner boundary location of the magnetospheric grid. We have also added a white circle in Figure 9c in order to facilitate visual comparison between the LFM-RCM results and those from the empirical model.

Visual comparison of the baseline and ET simulation results displayed in Figure 9 shows a similar shape and location of the inner magnetospheric pressure. The pressure is peaking inside of $4 R_E$. A detailed examination of pressure along midnight, not shown here, indicates that the ET pressure peaks $0.2 R_E$ closer to the Earth

than the baseline distribution. This difference is approximately the same as the inner magnetosphere cell sizes and is probably not significant. The peak pressure in the ET run is 10 nPa or 16% higher than the baseline simulation. This difference is significant and is likely the source of better agreement with the observed D_{ST} index shown in Figure 4c. The higher values for the peak pressure in the ET results are also improving the agreement with the peak pressures derived from the TS07d model.

Both of LFM-RCM simulation's pressure distributions are relatively symmetric about midnight. This is quite different from the TS07d data shown in Figure 9c which has peak in pressure in the premidnight sector. Along the midnight line a detailed examination of the pressure shows that it peaks at $2.9 R_E$, which is about $0.5 R_E$ closer to the Earth than the peak in either simulation result. Visual examination of the plots shows that the TS07d pressure distribution is more broad than either the baseline or ET simulations. In fact, looking again at the pressures along midnight, we find that the width TS07d pressure at half the maximum value is $1.2 R_E$ or 50% wider than either of the LFM-RCM simulation profiles.

It is worth noting that calculating the isotropic equilibrium pressure from the empirical magnetic field is not a trivial exercise, and many more efforts, including validation with in situ data, e.g., Van Allen Probes (VAP), will need to be carried out beyond the initial effort presented in Figure 9c. In particular, the amplitude of the pressure peak may be sensitive to the method of integration and boundary conditions. Nonetheless, our preliminary comparisons of the TS07d-reconstructed pressures with VAP demonstrated good agreement (not shown), and the pressure peak location is commensurate with the corresponding distribution of the $\vec{j} \times \vec{B}$ force in the model. In addition, the magnetic field configuration itself was validated extensively against VAP by *Stephens et al.* [2016]. Thus, we have some confidence in both the peak and location of the ring current pressure reconstructed from TS07d.

Considering the completely independent modeling approaches between LFM-RCM and TS07d (one physics based and the other empirical), it is quite remarkable that the magnitudes of the pressure peaks agree so well. The reasons for a more MLT symmetric pressure distribution in the LFM-RCM model will need to be investigated more carefully in a separate study. We hypothesize that the pressure distribution may be at least partly explained by the location of the RCM outer boundary controlled by the plasma beta [*Pembroke et al.*, 2012] and the resulting interplay of the $E \times B$ and gradient drifts that the coupled model allows between the plasma sheet and the ring current.

4. Discussion and Future Directions

In this work we have presented results from LFM-RCM simulations for a case study of a modest geomagnetic storm that occurred on 17 March 2013. These results include two significant changes to the LFM-RCM coupling from prior publications. First are the improvements to the LFM-RCM coupling methodology that allow it to deal with realistic solar wind conditions and dipole tilts. These changes place this version of the model on par with other models that couple global MHD simulations with the RCM and other ring current models. Second, we have implemented an electrojet turbulence model for modifying the ionospheric conductance. Generally speaking, this model parameterizes kinetic physics processes that are not possible to directly model in a global simulations and result in significantly higher conductances in regions of strong electric fields.

One common problem with LFM simulations in the past has been the high values of the CPCP relative to observations [e.g., *Gordeev et al.*, 2015], during strong solar wind driving conditions. The inclusion of the ET model in the LFM-RCM coupling results in significant reductions, on the order of 10%, in the CPCP during the strong driving conditions seen on 17 March 2013 geomagnetic storm. Even though the inclusion of ET into the simulation lowers the CPCP, it is clearly not sufficient to bring the simulated CPCP values to those observed [e.g., *Shepherd*, 2007]. Other sources of CPCP overestimation such as the representation of magnetic reconnection in the simulation will need to be considered. Equally important is the fact that the inclusion of the model does not result in changes to the CPCP during modest driving conditions. Also, we see that the enhancements to the conductance occur in the regions between the R1 and R2 currents flowing between the magnetosphere and ionosphere. This shifts the ET effects from the polar region to the electrojets providing a significant improvement over previous work by *Merkin et al.* [2005b] to include these processes. The improved representation of the R2 currents provided by the coupling with the RCM play an important role in both the location and magnitude of the ET effects.

Both baseline and ET simulation results show SAPS-like features when compared with the DMSP F18 observations. Inclusion of the ET effects produced significant improvements with the agreement to DMSP observations. The ET modules reduction of the CPCP help in bringing the cross-track ion velocities in better agreement with the DMSP observations. Also, the ET comparison of the 10:00 DMSP pass shows a double peaked feature that is in better agreement with the observations. Note that the predicted SAPS in both LFM-RCM simulation along the DMSP F18 pass is at the correct physical location, i.e., equatorward of the simulated auroral oval as shown in Figure 6, although the measured location of SAPS is approximately 4° equatorward in magnetic latitude in the premidnight sector compared to the simulated SAPS. It is possible that this discrepancy is a consequence of using an underinflated background magnetic field model as previously explained by *Burke et al.* [1998], which is a dipole field in the LFM-RCM simulation. Moreover, the dynamics of storm time ionospheric outflow may also play an important role in generating more realistic magnetic field topology especially in the plasma sheet [*Brambles et al.*, 2013], which is not included in the current LFM-RCM simulations. As demonstrated by *Raeder et al.* [2016], we need to include coupling with a physics-based ionosphere-thermosphere model to self-consistently model the midlatitude trough region associated with SAPS in order to improve our understanding of this coupled processes that drive SAPS.

In comparing the results of the simulations with field-aligned current observations made by AMPERE, we note minor differences between the two simulation results for the FAC magnitudes and patterns. In fact, during the peak of the initial strong driving interval the strength and location of the peaks of the R1 and R2 currents are not significantly different from each other even though there is a difference in the CPCP at this time. The lower CPCP in the ET results is due to the increased ionospheric conductance and the magnetosphere acting close to a constant current source at this time. The response of the MI coupled system is not linear such that the longer the interval of strong driving lasts, the greater is the difference between the currents, with the ET simulation having higher integrated current values. We have not focused heavily on the comparison of currents on the nightside since both simulations show more structure in the FAC patterns than can be gleaned from the AMPERE fit to the data. Although not at all times and not at all MLTs, the simulated currents tend to be located poleward of the observations. This feature is typically more pronounced on the nightside, where the simulated currents possess significant structure. The higher latitudes of the currents could be interpreted as a signature of an understretched magnetic field in the inner magnetosphere. However, the comparisons with ring current pressure between the simulation results and empirical reconstruction show relatively good agreement, so the reasons for this disparity need to be further investigated.

To test the state of the inner magnetosphere in the simulation, we have performed a comparison with the equilibrium isotropic pressure reconstructed from the TS07d empirical model of the magnetic field. The comparison between the two simulations shows little differences in terms of the structure or widths of the ring current pressure distribution in the inner magnetosphere. The ET simulation did have a 16% higher peak pressure, which was closer to the values derived from the TS07d model. In the simulation results the ring current pressure was rather symmetric with a peak near midnight, while the TS07d model pressure has a premidnight peak. However, we note that the agreement of the peak pressures between the physics-based and empirical models is quite remarkable considering that they are two completely independent methods of the reconstruction of the magnetospheric state. The comparison presented in this paper is a preliminary effort in the direction of what we view as a very powerful tool for validation of global models. Inner magnetosphere pressure is a quantity that is very important for inferring the global state of the storm time magnetosphere since it regulates the generation of R2 currents and inflation of the geomagnetic field. At the same time, recovering its global distribution and, in particular, the location of the pressure peak, is difficult from in situ data [e.g., *Gkioulidou et al.*, 2014], whereas global reconstructions, e.g., from energetic neutral atom (ENA) images [*Brandt et al.*, 1359] lack resolution and have substantial uncertainties. Thus, the empirical pressure reconstruction promises to be a highly useful tool for not only validation but also potential adjustment of inner magnetosphere pressures in global models. However, these reconstructions should first also undergo validation using in situ measurements and then much more detailed comparisons with global MHD simulations should be undertaken. We defer such a detailed analysis to a dedicated publication.

These initial results from the extension of the LFM-RCM show good agreement with a range of observations and notable improvements when the ET-driven enhancements to ionospheric conductivity are included. They also point to several interesting directions for more detailed analysis. The capturing of the SAPS structures needs to be examined in more detail across a broader range of driving conditions. Particular attention needs to be paid to investigate what regulates when and where these structures are seen in the simulation results.

Future investigations are needed to establish a system-level understanding on the SAPS phenomenon using the coupled LFM-RCM model, including incorporating the feedback effect from ionospheric plasma chemical processes and thermospheric neutral dynamics using the fully coupled LFM-RCM-TIEGCM code. The evolution of the ring current pressures over this and other storms also requires more investigation. In particular, it is important to understand what determines the radial extent of the pressure distribution in the simulation as well as the radial and azimuthal location of the pressure peak.

Finally, as noted above, our ultimate goal in this project is to combine the work using LFM-RCM simulations presented here with the modeling that includes ET effects in the simulations of ionosphere-thermosphere self-consistently [Liu *et al.*, 2016]. This work is currently underway and will be presented in a future publication. This fully coupled version of the model will also allow us to make comparisons with plasmasphere erosion measurements reported by Foster *et al.* [2014].

Acknowledgments

This material is based upon work supported by NASA grants NNX14AI13G, NNX13AF92G, and NNX16AB80G. The National Center for Atmospheric Research is sponsored by the National Science Foundation. This work used the XSEDE and TACC computational facilities, supported by National Science Foundation grant ACI-1053575. We would like to acknowledge high-performance computing support from Yellowstone (ark:/85065/d7wd3xhc) provided by NCAR's Computational and Information Systems Laboratory, sponsored by the National Science Foundation. We thank the AMPERE team and the AMPERE Science Center for providing the Iridium derived data products. All model output, simulation codes, and analysis routines are being preserved on the NCAR High-Performance Storage System and will be made available upon written request to the lead author of this publication.

References

- Anderson, B. J., H. Korth, D. T. Welling, V. G. Merkin, M. J. Wiltberger, J. Raeder, R. J. Barnes, C. L. Waters, A. A. Pulkkinen, and L. Rastaetter (2016), Comparison of predictive estimates of high latitude electrodynamics with observations of global scale birkeland currents, *Space Weather*, 15(2), 352–373, doi:10.1002/2016SW001529.
- Bahcivan, H. (2007), Plasma wave heating during extreme electric fields in the high-latitude *E* region, *Geophys. Res. Lett.*, 34, L15106, doi:10.1029/2006GL029236.
- Balsley, B. B., and D. T. Farley (1971), Radar studies of the equatorial electrojet at three frequencies, *J. Geophys. Res.*, 76(3), 8341–8351, doi:10.1029/JA076i034p08341.
- Brambles, O. J., W. Lotko, B. Zhang, J. Ouellette, J. Lyon, and M. Wiltberger (2013), The effects of ionospheric outflow on ICME and SIR driven sawtooth events, *J. Geophys. Res. Space Physics*, 118, 6026–6041, doi:10.1002/jgra.50522.
- Brandt, P., C. Son, D. G. Mitchell, Y. Ebihara, B. R. Sandel, E. C. Roelof, J. L. Burch, and R. Demajistre (1959), Global IMAGE/HENA observations of the ring current: Examples of rapid response to IMF and ring current-plasmasphere interaction, *J. Geophys. Res.*, 107, doi:10.1029/2001JA000084.
- Buchert, S. C., T. Hagfors, and J. F. McKenzie (2006), Effect of electrojet irregularities on DC current flow, *J. Geophys. Res.*, 111, A02305, doi:10.1029/2004JA010788.
- Buneman, O. (1963), Excitation of field aligned sound waves by electron streams, *Phys. Rev. Lett.*, 10(7), 285–287, doi:10.1103/PhysRevLett.10.285.
- Burke, W. J., N. C. Maynard, M. P. Hagan, R. A. Wolf, G. R. Wilson, L. C. Gentile, M. S. Gussenhoven, T. C. Y. Huang, W. Garner, and F. J. Rich (1998), Electrodynamics of the inner magnetosphere observed in the dusk sector by CRRES and DMSP during the magnetic storm of June 4–6, 1991, *J. Geophys. Res.*, 103, 29,399–29,418, doi:10.1029/98JA02197.
- Cohen, R., and K. L. Bowles (1967), Secondary irregularities in the equatorial electrojet, *J. Geophys. Res.*, 72(3), 885–894, doi:10.1029/JZ072i003p0885.
- Coroniti, F. V., and C. F. Kennel (1973), Can the ionosphere regulate magnetospheric convection?, *J. Geophys. Res.*, 78(16), 2837–2851, doi:10.1029/JA078i016p02837.
- Crochet, M., C. Hanuise, and P. Broche (1979), HF radar studies of two-stream instability during an equatorial counter-electrojet, *J. Geophys. Res.*, 84(A9), 5223–5233, doi:10.1029/JA084iA09p05223.
- De Zeeuw, D. L., S. Sazykin, R. A. Wolf, T. I. Gombosi, A. J. Ridley, and G. Tóth (2004), Coupling of a global MHD code and an inner magnetospheric model: Initial results, *J. Geophys. Res.*, 109, A12219, doi:10.1029/2003JA010366.
- Dimant, Y. S., and G. M. Milikh (2003), Model of anomalous electron heating in the *E* region: 1. Basic theory, *J. Geophys. Res.*, 108, A1350, doi:10.1029/2002JA009524.
- Dimant, Y. S., and M. M. Oppenheim (2011a), Magnetosphere-ionosphere coupling through *E* region turbulence: 1. Energy budget, *J. Geophys. Res.*, 116, A09303, doi:10.1029/2011JA016648.
- Dimant, Y. S., and M. M. Oppenheim (2011b), Magnetosphere-ionosphere coupling through *E* region turbulence: 2. Anomalous conductivities and frictional heating, *J. Geophys. Res.*, 116, A09304, doi:10.1029/2011JA016649.
- Farley, D. T. J. (1963), A plasma instability resulting in field-aligned irregularities in the ionosphere, *J. Geophys. Res.*, 68(22), 6083–6097, doi:10.1029/JZ068i022p06083.
- Fedder, J. A., J. G. Lyon, S. P. Slinker, and C. M. Mobarry (1995a), Topological structure of the magnetotail as a function of interplanetary magnetic field direction, *J. Geophys. Res.*, 100(A3), 3613–3621, doi:10.1029/94JA02577.
- Fedder, J. A., S. P. Slinker, J. G. Lyon, and R. D. Elphinstone (1995b), Global numerical simulation of the growth phase and the expansion onset for a substorm observed by Viking, *J. Geophys. Res.*, 100, 19,083–19,094, doi:10.1029/95JA01524.
- Foster, J. C., and P. J. Erickson (2000), Simultaneous observations of *E*-region coherent backscatter and electric field amplitude at *F*-region heights with the Millstone Hill UHF radar, *Geophys. Res. Lett.*, 27(19), 3177–3180, doi:10.1029/2000GL000042.
- Foster, J. C., P. J. Erickson, A. J. Coster, S. Thaller, J. Tao, J. R. Wygant, and J. W. Bonnell (2014), Storm time observations of plasmasphere erosion flux in the magnetosphere and ionosphere, *Geophys. Res. Lett.*, 41, 762–768, doi:10.1002/2013GL059124.
- Fukao, S., M. Yamamoto, R. T. Tsunoda, H. Hayakawa, and T. Mukai (1998), The SEEK (Sporadic-*E* Experiment over Kyushu) campaign, *Geophys. Res. Lett.*, 25(11), 1761–1764, doi:10.1029/98GL00932.
- Gallagher, D. L., P. D. Craven, and R. H. Comfort (2000), Global core plasma model, *J. Geophys. Res.*, 105(A8), 18,819–18,833, doi:10.1029/1999JA000241.
- Gkioulidou, M., A. Y. Ukhorskiy, D. G. Mitchell, T. Sotirelis, B. H. Mauk, and L. J. Lanzerotti (2014), The role of small-scale ion injections in the buildup of Earth's ring current pressure: Van Allen Probes observations of the 17 March 2013 storm, *J. Geophys. Res. Space Physics*, 119, 7327–7342, doi:10.1002/2014JA020096.
- Goodrich, C. C., A. L. Sussman, J. G. Lyon, M. A. Shay, and P. A. Cassak (2004), The CISM code coupling strategy, *J. Atmos. Sol. Terr. Phys.*, 66(1), 1469–1479, doi:10.1016/j.jastp.2004.04.010.
- Gordeev, E., V. Sergeev, I. Honkonen, M. Kuznetsova, L. Rastätter, M. Palmroth, P. Janhunen, G. Tóth, J. Lyon, and M. Wiltberger (2015), Assessing the performance of community-available global MHD models using key system parameters and empirical relationships, *Space Weather*, 13(1), 868–884, doi:10.1002/2015SW001307.

- Gurevich, A. V. (1978), *Nonlinear Phenomena in the Ionosphere*, vol. 10, Spring, New York.
- Hapgood, M. A. (1992), Space physics coordinate transformations: A user guide, *Planet. Space Sci.*, 40, 711–717, doi:10.1016/0032-0633(92)90012-D.
- Hassan, E., W. Horton, A. I. Smolyakov, D. R. Hatch, and S. K. Litt (2015), Multiscale equatorial electrojet turbulence: Baseline 2-D model, *J. Geophys. Res. Space Physics*, 120, 1460–1477, doi:10.1002/2014JA020387.
- Hill, T. W., A. J. Dessler, and R. A. Wolf (1976), Mercury and Mars: The role of ionospheric conductivity in the acceleration of magnetospheric particles, *Geophys. Res. Lett.*, 3(8), 429–432, doi:10.1029/GL003i008p00429.
- Janhunen, P. (1996), GUMICS-3—A global ionosphere-magnetosphere coupling simulation with high ionospheric resolution, in *Proceedings ESA 1996 Symposium on Environment Modelling for Space-based Applications ESA SP-392*, edited by W. Burke and T.-D. Guyenne, pp. 233, ESTEC, Noordwijk, Netherlands.
- Kelley, M. C. (1989), *The Earth's Ionosphere*, International Geophysics Series, Academic Press, San Diego, Calif.
- Kovalev, D. V., A. P. Smirnov, and Y. S. Dimant (2008), Modeling of the Farley-Buneman instability in the E-region ionosphere: A new hybrid approach, *Ann. Geophys.*, 26(9), 2853–2870, doi:10.5194/angeo-26-2853-2008.
- Kudeki, E., B. G. Fejer, D. T. Farley, and C. Hanuise (1987), The Condor equatorial electrojet campaign: Radar results, *J. Geophys. Res.*, 92, 13561–13577.
- Li, Z., M. Hudson, J. Paral, M. Wiltberger, and D. Turner (2016), Global ULF wave analysis of radial diffusion coefficients using a global MHD model for the 17 March 2015 storm, *J. Geophys. Res. Space Physics*, 121, 6196–6206, doi:10.1002/2016JA022508.
- Liu, J., W. Wang, M. Oppenheim, Y. Dimant, M. Wiltberger, and S. Merkin (2016), Anomalous electron heating effects on the E region ionosphere in TIEGCM, *Geophys. Res. Lett.*, 43, 2351–2358, doi:10.1002/2016GL068010.
- Merkin, V. G., and J. G. Lyon (2010), Effects of the low-latitude ionospheric boundary condition on the global magnetosphere, *J. Geophys. Res.*, 115, A10202, doi:10.1029/2010JA015461.
- Merkin, V. G., A. S. Sharma, K. Papadopoulos, G. Milikh, J. Lyon, and C. Goodrich (2005a), Global MHD simulations of the strongly driven magnetosphere: Modeling of the transpolar potential saturation, *J. Geophys. Res.*, 110, A9203, doi:10.1029/2004JA010993.
- Merkin, V. G., G. Milikh, K. Papadopoulos, J. Lyon, Y. S. Dimant, A. S. Sharma, C. Goodrich, and M. Wiltberger (2005b), Effect of anomalous electron heating on the transpolar potential in the LFM global MHD model, *Geophys. Res. Lett.*, 32, L22101, doi:10.1029/2005GL023315.
- Merkin, V. G., B. J. Anderson, J. G. Lyon, H. Korth, M. Wiltberger, and T. Motoba (2013), Global evolution of Birkeland currents on 10 min timescales: MHD simulations and observations, *J. Geophys. Res. Space Physics*, 118, 4977–4997, doi:10.1002/jgra.50466.
- Merkine, V. G., K. Papadopoulos, G. Milikh, A. S. Sharma, X. Shao, J. Lyon, and C. Goodrich (2003), Effects of the solar wind electric field and ionospheric conductance on the cross polar cap potential: Results of global MHD modeling, *Geophys. Res. Lett.*, 30(2), 2180, doi:10.1029/2003GL017903.
- Milikh, G. M., and Y. S. Dimant (2002), Kinetic model of electron heating by turbulent electric field in the E region, *Geophys. Res. Lett.*, 29(12), 1575, doi:10.1029/2001GL013935.
- Milikh, G. M., and Y. S. Dimant (2003), Model of anomalous electron heating in the E region: 2. Detailed numerical modeling, *J. Geophys. Res.*, 108(A9), 1351, doi:10.1029/2002JA009527.
- Milikh, G. M., L. Goncharenko, Y. S. Dimant, J. P. Thayer, and M. A. McCready (2006), Anomalous electron heating and its effect on the electron density in the auroral electrojet, *Geophys. Res. Lett.*, 33, L13809, doi:10.1029/2006GL026530.
- Moen, J., and A. Brekke (1993), The solar flux influence on quiet time conductances in the auroral ionosphere, *Geophys. Res. Lett.*, 20, 971–974, doi:10.1029/92GL02109.
- Ohtani, S., S. Wing, V. G. Merkin, and T. Higuchi (2014), Solar cycle dependence of nightside field-aligned currents: Effects of dayside ionospheric conductivity on the solar wind-magnetosphere-ionosphere coupling, *J. Geophys. Res. Space Physics*, 119, 322–334, doi:10.1002/2013JA019410.
- Oppenheim, M. (1996), A wave-driven nonlinear current in the E-region ionosphere, *Geophys. Res. Lett.*, 23, 3333–3336, doi:10.1029/96GL03100.
- Oppenheim, M. (1997), Evidence and effects of a wave-driven nonlinear current in the equatorial electrojet, *Ann. Geophys.*, 15(7), 899–907, doi:10.1007/s00585-997-0899-z.
- Oppenheim, M. M., and Y. S. Dimant (2013a), Kinetic simulations of 3-D Farley-Buneman turbulence and anomalous electron heating, *J. Geophys. Res. Space Physics*, 118, 1306–1318, doi:10.1002/jgra.50196.
- Oppenheim, M. M., and Y. S. Dimant (2013b), Kinetic simulations of 3-D Farley-Buneman turbulence and anomalous electron heating, *J. Geophys. Res. Space Physics*, 118, 1306–1318, doi:10.1002/jgra.50196.
- Oppenheim, M. M., Y. Dimant, and L. P. Dyrud (2008), Large-scale simulations of 2-D fully kinetic Farley-Buneman turbulence, *Ann. Geophys.*, 26(3), 543–553, doi:10.5194/angeo-26-543-2008.
- Pembroke, A., F. Toffoletto, S. Sazykin, M. Wiltberger, J. Lyon, V. Merkin, and P. Schmitt (2012), Initial results from a dynamic coupled magnetosphere-ionosphere-ring current model, *J. Geophys. Res.*, 117, A02211, doi:10.1029/2011JA016979.
- Pfaff, R. F., M. C. Kelley, E. Kudeki, B. G. Fejer, and K. D. Baker (1987), Electric field and plasma density measurements in the strongly driven daytime equatorial electrojet: 2. Two-stream waves, *J. Geophys. Res.*, 92(A12), 13,597–13,612, doi:10.1029/JA092iA12p13597.
- Providakes, J., D. T. Farley, B. G. Fejer, J. Sahr, W. E. Swartz, I. Häggström, A. Hedberg, and J. A. Nordling (1988), Observations of auroral E-region plasma waves and electron heating with EISCAT and a VHF radar interferometer, *J. Atmos. Terr. Phys.*, 50(4–5), 339,349–347,356, doi:10.1016/0021-9169(88)90019-0.
- Raeder, J. (2003), Global magnetohydrodynamics—A tutorial, in *Space Plasma Simulation*, vol. 615, edited by J. Büchner, C. T. Dum, and M. Scholer, pp. 212–246, Springer, New York.
- Raeder, J., R. J. Walker, and M. Ashour-Abdalla (1995), The structure of the distant geomagnetic tail during long periods of northward IMF, *Geophys. Res. Lett.*, 22(4), 349–352, doi:10.1029/94GL03380.
- Raeder, J., R. L. McPherron, L. A. Frank, S. Kokubun, G. Lu, T. Mukai, W. R. Paterson, J. B. Sigwarth, H. J. Singer, and J. A. Slavin (2001), Global simulation of the Geospace Environment Modeling substorm challenge event, *J. Geophys. Res.*, 106(A1), 381–395, doi:10.1029/2000JA000605.
- Raeder, J., W. D. Cramer, J. Jensen, T. Fuller-Rowell, N. Maruyama, F. Toffoletto, and H. Vo (2016), Sub-auroral polarization streams: A complex interaction between the magnetosphere, ionosphere, and thermosphere, *J. Phys. Conf. Ser.*, 767(1), 012021, doi:10.1088/1742-6596/767/1/012021.
- Rasmussen, C. E., R. W. Schunk, and V. B. Wickwar (1988), A photochemical equilibrium model for ionospheric conductivity, *J. Geophys. Res.*, 93(A9), 9831–9840, doi:10.1029/JA093iA09p09831.
- Richmond, A. D. (1992), Assimilative mapping of ionospheric electrodynamics, *Adv. Space Res.*, 12(6), 59–68, doi:10.1016/0273-1177(92)90040-5.

- Ridley, A., T. Gombosi, and D. DeZeeuw (2004), Ionospheric control of the magnetosphere: Conductance, *Ann. Geophys.*, 22(2), 567–584, doi:10.5194/angeo-22-567-2004.
- Rogister, A., and E. Jamin (1975), Two-dimensional nonlinear processes associated with 'type 1' irregularities in the equatorial electrojet, *J. Geophys. Res.*, 80(13), 1820–1828, doi:10.1029/JA080i013p01820.
- Rose, G., K. Schlegel, K. Rinnert, H. Kohl, E. Nielsen, G. Dehm, A. Friker, F. J. Lübken, H. Lühr, E. Neske, and A. Steinweg (1992), The ROSE project. Scientific objectives and discussion of first results, *J. Atmos. Terr. Phys.*, 54(6), 657–667, doi:10.1016/0021-9169(92)90104-S.
- Schlegel, K. (1982), Reduced effective recombination coefficient in the disturbed polar E-region, *J. Atmos. Terr. Phys.*, 44(2), 183–185, doi:10.1016/0021-9169(82)90121-0.
- Schlegel, K., and J. P. St Maurice (1981), Anomalous heating of the polar E region by unstable plasma waves 1. Observations, *J. Geophys. Res.*, 86(A3), 1447–1452, doi:10.1029/JA086iA03p01447.
- Sergeev, V. A., T. I. Pulkkinen, T. I. Pellinen, and N. A. Tsyganenko (1994), Hybrid state of the tail magnetic configuration during steady convection events, *J. Geophys. Res.*, 99(A12), 23,571–23,582, doi:10.1029/94JA01980.
- Shepherd, S. G. (2007), Polar cap potential saturation: Observations, theory, and modeling, *J. Atmos. Sol. Terr. Phys.*, 69(3), 234–248, doi:10.1016/j.jastp.2006.07.022.
- Siscoe, G., G. Erickson, B. Sonnerup, and N. Maynard (2002a), Hill model of transpolar potential saturation: Comparisons with MHD simulations, *J. Geophys. Res.*, 107(A6), 1075, doi:10.1029/2001JA000109.
- Siscoe, G. L., N. U. Crooker, and K. D. Siebert (2002b), Transpolar potential saturation: Roles of region 1 current system and solar wind ram pressure, *J. Geophys. Res.*, 107, A1321, doi:10.1029/2001JA009176.
- Sitnov, M. I., N. A. Tsyganenko, A. Y. Ukhorskiy, and P. C. Brandt (2008), Dynamical data-based modeling of the storm-time geomagnetic field with enhanced spatial resolution, *J. Geophys. Res.*, 113, A07218, doi:10.1029/2007JA013003.
- St Maurice, J. P. (1990), Electron heating by plasma waves in the high latitude E-region and related effects: Theory, *COSPAR*, 10(6), 239–249, doi:10.1016/0273-1177(90)90257-Z.
- St Maurice, J. P., and R. Laher (1985), Are observed broadband plasma wave amplitudes large enough to explain the enhanced electron temperatures of the high-latitude E region?, *J. Geophys. Res.*, 90(A3), 2843–2850, doi:10.1029/JA090iA03p02843.
- Stauning, P., and J. K. Olesen (1989), Observations of the unstable plasma in the disturbed polar E-region, *Phys. Scr.*, 40(3), 325–332, doi:10.1088/0031-8949/40/3/012.
- Stephens, G. K., M. I. Sitnov, J. Kissinger, N. A. Tsyganenko, R. L. McPherron, H. Korth, and B. J. Anderson (2013), Empirical reconstruction of storm time steady magnetospheric convection events, *J. Geophys. Res. Space Physics*, 118, 6434–6456, doi:10.1002/jgra.50592.
- Stephens, G. K., M. I. Sitnov, A. Y. Ukhorskiy, E. C. Roelof, N. A. Tsyganenko, and G. Le (2016), Empirical modeling of the storm time innermost magnetosphere using Van Allen Probes and THEMIS data: Eastward and banana currents, *J. Geophys. Res. Space Physics*, 121, 157–170, doi:10.1002/2015JA021700.
- Toffoletto, F. R., S. Sazykin, R. W. Spiro, and R. A. Wolf (2003), Inner magnetosphere modeling with the Rice Convection Model, *Space Sci. Rev.*, 107, 175–196.
- Tsyganenko, N. A. (1995), Modeling the Earth's magnetospheric magnetic field confined within a realistic magnetopause, *J. Geophys. Res.*, 100, 5599–5612, doi:10.1029/94JA03193.
- Tsyganenko, N. A., and M. I. Sitnov (2007), Magnetospheric configurations from a high-resolution data-based magnetic field model, *J. Geophys. Res.*, 112, A06225, doi:10.1029/2007JA012260.
- Welling, D. T., and A. J. Ridley (2010), Validation of SWMF magnetic field and plasma, *Space Weather*, 8, S03002, doi:10.1029/2009SW000494.
- Wiltberger, M., R. S. Weigel, W. Lotko, and J. A. Fedder (2009), Modeling seasonal variations of auroral particle precipitation in a global-scale magnetosphere-ionosphere simulation, *J. Geophys. Res.*, 114, A01204, doi:10.1029/2008JA013108.
- Wolf, R. A. (1983), The quasi-static (slow-flow) region of the magnetosphere, in *Solar Terrestrial Physics*, edited by R. L. Carovillano and J. M. Forbes, pp. 303–368, Springer, D. Reidel Publ. Co., Hingham, MA.
- Zanetti, L. J., T. A. Potemra, P. F. Bythrow, T. Iijima, and W. Baumjohann (1984), Ionospheric and Birkeland current distributions for northward interplanetary magnetic field—Inferred polar convection, *J. Geophys. Res.*, 89(A9), 7453–7458, doi:10.1029/JA089iA09p07453.
- Zhang, B., W. Lotko, M. J. Wiltberger, O. J. Brambles, and P. A. Damiano (2011), A statistical study of magnetosphere-ionosphere coupling in the Lyon-Fedder-Mobarry global MHD model, *J. Atmos. Sol. Terr. Phys.*, 73(5), 686–702, doi:10.1016/j.jastp.2010.09.027.